Advanced Steel Construction – Vol. 21 No. 1 (2025) 31–41
DOI:10.18057/IJASC.2025.21.1.3

STUDY ON BENDING PERFORMANCE AND LOAD-CARRYING CAPACITY OF SINGLE-LAYER CYLINDRICAL RETICULATED SHELL WITH NEW SPRAYER JOINT

Ren Li, Jun-Ji Jin, Zhi-Cheng Xiao, Shou-Fang Jiang and Hui-Jun Li *

College of Water Resources and Architectural Engineering, Northwest A&F University, Shaanxi Yangling, 712100
** (Corresponding author: E-mail: lihuijun2893118@163.com)*

ABSTRACT

The bending stiffness of joints is a critical factor that impacts the bearing capacity of large-span spatial reticulated shell structures. To address the issue of relatively low bending stiffness of traditional socket joints, a novel type of sprayer joint is introduced in this study. Initially, the bending performance of the socket joint is validated, leading to the proposal of the sprayer joint. Then, a refined finite element model is established to investigate the bending performance of the sprayer joints with varying surrounding bolt radii under axial tension and compression loads. Subsequently, an improved bilinear model is developed to effectively determine the bending performance with precise yield position. Finally, the comparative performance of the new sprayer joint and the traditional socket joint in single-layer cylindrical reticulated shells is studied in detail. The findings indicate that the bending performance of the new sprayer joint surpasses that of the traditional socket joint, and the ultimate load of the new sprayer joint reticulated shell has significantly increased compared to the traditional socket joint, highlighting the efficiency and success of the new sprayer joint design. Moreover, it is observed that axial compression and the radius of surrounding bolts can enhance the bending performance, while axial tension exhibits opposite effect. The failure mode of the new sprayer joint is elucidated, and the improved bilinear model accurately describes the yield position and bending process of the joint. These conclusions offer valuable insights for the structural design and application of the sprayer joint.

ARTICLE HISTORY

Received: 28 February 2024
Revised: 12 November 2024
Accepted: 30 November 2024

KEYWORDS

Bending stiffness;
Spatial reticulated shell structures;
New sprayer joint;
Improved bilinear model

1. Introduction

Joint stiffness, particularly bending stiffness, is a critical factor that impacts the stability, bearing capacity, and failure mode of reticulated shells [1-3]. Recent researches have primarily focused on bending stiffness, bearing capacity, and failure mode of semi-rigid joints [4-26]. Research has been conducted, including extensive experimental, numerical, and theoretical studies. Fan *et al.* [27] conducted experiments on bolted-ball joints under combined compression and bending loads. The refined numerical analysis model has been developed for semi-rigid joints that considers axial pressure and bolt preload, and determined the rotational stiffness and ultimate bearing capacity of joints under compression and bending. Zhang *et al.* [28] delved into the bending performance of embedded hub joints, utilizing a power function model to analyze the bending moment-rotation relationship and its impact on the bearing capacity of single-layer spherical reticulated shells. Guo *et al.* [29] performed experimental investigations on plate joints, examining the failure modes under varying plate thicknesses and noting an increase in joint stiffness with thicker plates.

The traditional socket joint (shown in Fig.1) is commonly utilized in large-span spatial reticulated shell structures due to its simple assembly, convenient construction, and aesthetic appeal [30, 31]. However, for spatial reticulated shell structures with larger spans, the bending stiffness of the traditional bowl joint is insufficient, measuring only about 20% of the Temcor joint [30, 32]. Therefore, enhancing the bending stiffness of traditional socket joint to accommodate larger spans is crucial. The bending moment-rotation curve of semi-rigid joints serves as a key index of their mechanical properties. To simplify calculations, scholars have proposed various mathematical models. Current moment-rotation curve models include linear, bilinear, polynomial, B-spline, power function, exponential function, and trilinear models [33-37]. The bilinear and trilinear models are commonly used in calculating reticulated shell structures, although issues regarding accuracy still exist, particularly in accurately describing the bearing capacity at nonlinear stage and the yield point of the bending moment-rotation curve.

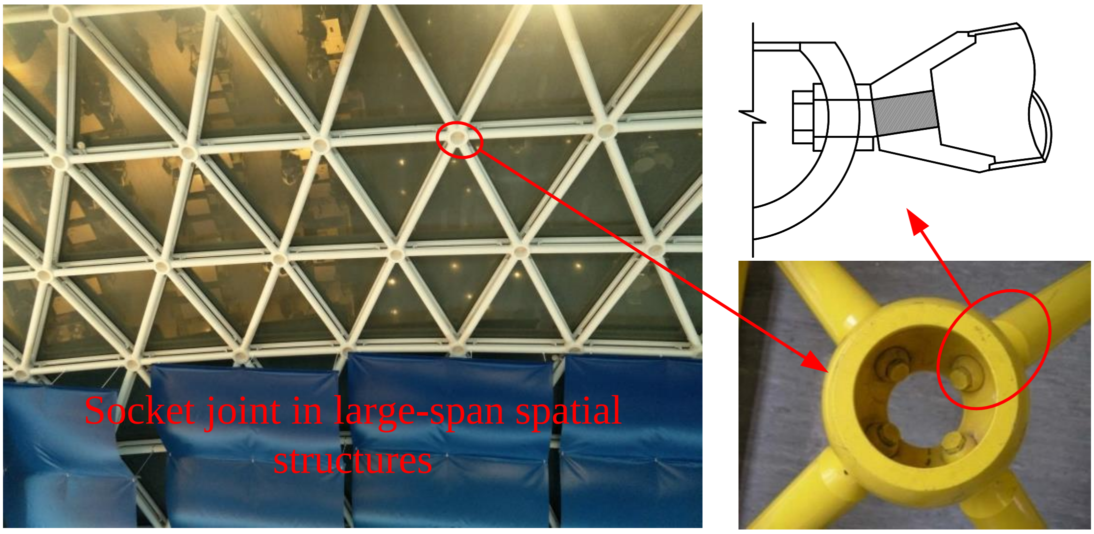

Fig. 1 Socket joint in large-span spatial structures

To address the aforementioned challenges, this study initially validates the bending performance of the socket joint and introduces a new sprayer joint. To evaluate the bending performance of the joint, a refined finite element model was developed to analyze the bending performance of sprayer joints with varying surrounding bolt radii under axial tension and compression loads. Subsequently, an improved bilinear model is proposed which can effectively depicts the bearing capacity at nonlinear stage and the yield point of the bending moment-rotation curve. Finally, the comparative performance of the new sprayer joint and the traditional socket joint in single-layer cylindrical reticulated shells is studied in detail.

2. Establishment of FE model of the new sprayer joint and comparison with socket joint

Traditional socket joint exhibits relatively weak bending stiffness due to its less bending moment resistance [30], a new type of spray joint is proposed to improve the bending stiffness of the conventional joint [38]. The sprayer joint introduced in this study is composed of a bowl-shaped steel hollow ball with a welded cylinder (sprayer body), washers, a central bolt, four surrounding bolts, and a sprayer cone. The assembly and configuration of the sprayer joint are depicted in Fig. 2.

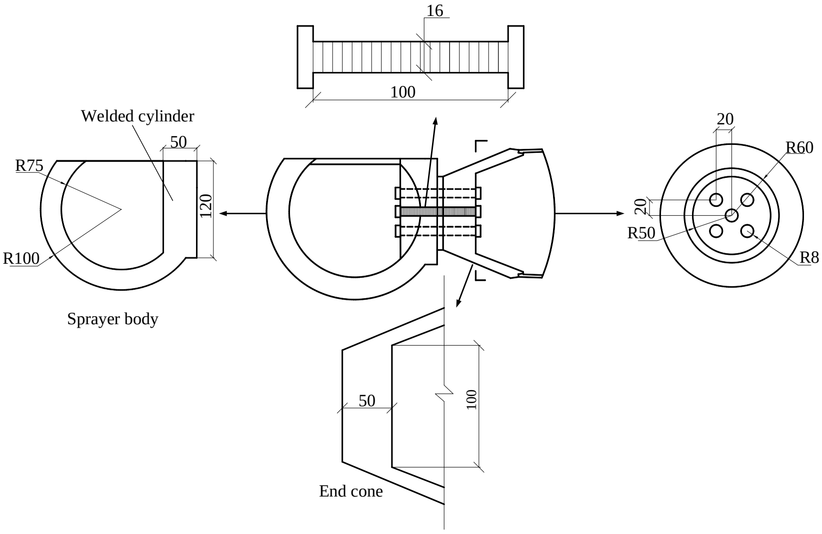

Fig. 2 Assembly and configuration of the sprayer joint (unit: mm)

In order to investigate the bending performance of the novel sprayer joint, refined FE model was constructed for both the traditional socket joint and the new sprayer one in ABAQUS package. Each joint component was simulated using the secondary reduced integration solid element (C3D8R). The meshed joint model is depicted in Fig. 3, with a total of 42472 elements and 65104 nodes. To accurately capture the stress distribution of the joint, 17 contact pairs are established, as shown in Table 1. The material property parameters for each joint component are outlined in Table 2, and the bilinear constitutive relation was used in the FE model. To reduce the computational effort, half of the finite element model (left side) was applied fixed constraints due to the symmetry of the new sprayer node. A bolt preload of 100kN was applied to both the traditional socket joint and the new sprayer-type one, with the joint achieving its ultimate bearing capacity under pure bending (a specific bending moment applied to the cone section).

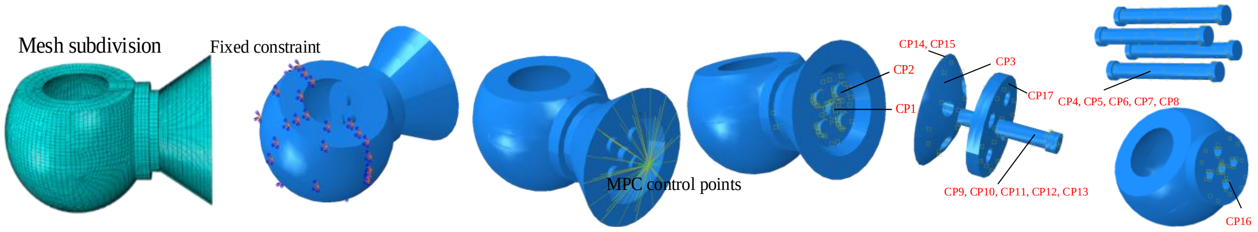

Fig. 3 Refined finite element model of sprayer joint

Table 1
Contact pair settings

Contact pairs	Master surface	Slave surface
CP1	End cone-down	Central bolt-down
CP2	End cone-down	Surrounding bolt-down
CP3	Sprayer body-inside	Washer 1
CP4	Washer 1-hole	Central bolt-side
CP5	Washer 2-hole	Central bolt-side
CP6	End cone-hole	Central bolt-side
CP7	Welded cylinder-hole	Central bolt-side
CP8	Sprayer body-hole	Central bolt-side
CP9	Washer 1-hole	Surrounding bolt-side
CP10	Washer 2-hole	Surrounding bolt-side
CP11	End cone-hole	Surrounding bolt-side
CP12	Welded cylinder-hole	Surrounding bolt-side
CP13	Sprayer body-hole	Surrounding bolt-side
CP14	Washer 1	Central bolt-up
CP15	Washer 1	Surrounding bolt-up
CP16	Welded cylinder	Washer 1
CP17	End cone	Washer 2

Table 2
Material property parameters [31,38]

Assembly part	*E*	*v*	$f_{0.2}$	*ρ*
Sprayer body of sprayer joint	2.06×10^5MPa	0.3	328MPa	7850kg/m^3
Bowl-joint ball of socket			328MPa	
Bolts of sprayer joint			684MPa	
Bolt of socket			684MPa	
End cone of sprayer joint			405MPa	
End cone of socket			405MPa	

The numerical simulation results of the traditional socket joint were obtained and compared with the experimental results to validate the model used in this study [31]. Fig. 4 displays the moment-rotation curve, showing a satisfactory agreement between the finite element results and the experimental results of traditional socket joints. This alignment serves to validate the accuracy of the finite element model. Fig. 4 presents a comparative diagram of the bending moment-rotation curve for both the new sprayer joint and the traditional socket joint. It is evident that the bending performance of the new sprayer joint exhibits significant enhancement as compared to the traditional socket joint.

According to the moment-rotation curve (Fig. 4), it is evident that the bending performance of the novel sprayer joint surpasses that of the socket joint. The failure mode of the joint is illustrated in Fig. 5, revealing that, prior to joint failure, the lower part of the surrounding bolt experiences initial tension and yielding, which increases the resistance moment of the joint. The ductility of the joint is inferior to that of the traditional socket joint. To delve into its failure mechanism and bending performance, the bending performance of the sprayer joint with varying bolt radii is further examined in the next section.

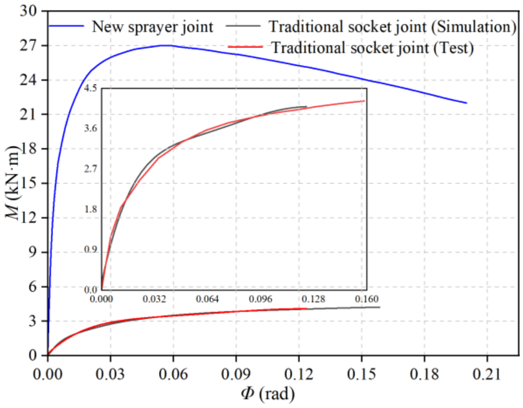

Fig. 4 Verification of numerical model and comparison on bending moment-rotation curve with socket joint

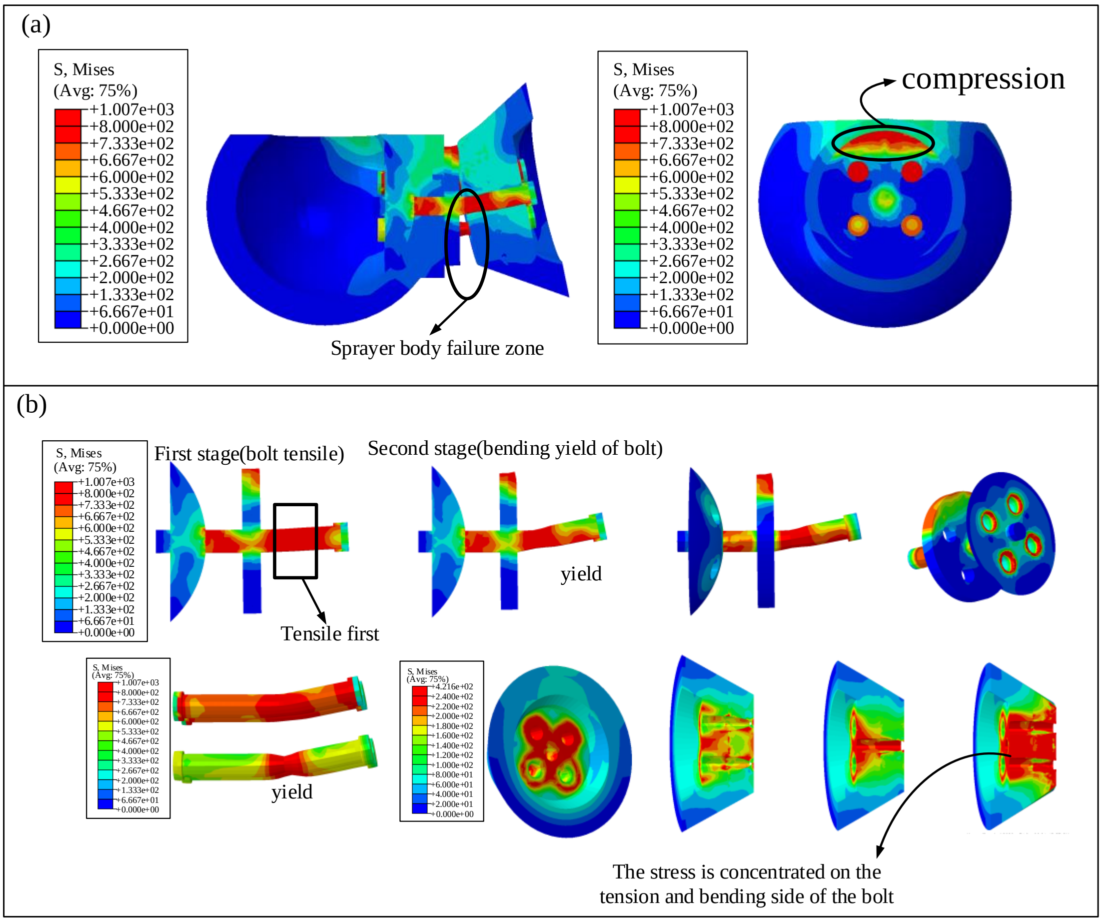

Fig. 5 Mises stress contour and failure mode of the new sprayer joint

3. Bending performance of the new sprayer joint with different diameters of surrounding bolts under axial compression and tension

3.1. Bending properties

From Fig. 6 it can be seen that as the diameter of the surrounding bolts increases, the stress value in the yield region gradually decreases in the ultimate failure state. Additionally, the yield point of the surrounding bolts moves from positions *A* to *B*. When the diameter of the surrounding bolts exceeds 9mm, the bolts no longer neck in the ultimate state. Instead, the surrounding bolts of lower side and the joints bend and yield simultaneously. When the joint is subjected to a bending moment, the tension side bolt and the cylinder compression area form a resistance bending moment. If applied bending moment is less than the rotational capacity, the joint will not experience significant rotation. At this point, the smaller diameter bolt of the tension side will reach ultimate strength. The analysis above demonstrates that the cylinder and surrounding bolts of the new sprayer joint can enhance the bending stiffness of the joint. Table 3 shows that compared to the socket joint with an 8mm surrounding bolt, the new joint, with the same size surrounding bolt, has an increased initial stiffness by 21.71 times and an increased ultimate bearing capacity by 5.42 times, with only a 15% increase in steel consumption. Consequently, the surrounding bolts with larger diameters provide greater resistance to bending moment and significantly improve the ultimate bearing capacity of the joint.

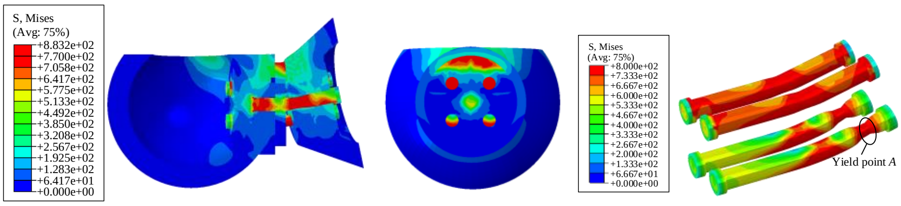

(a) BD8-7

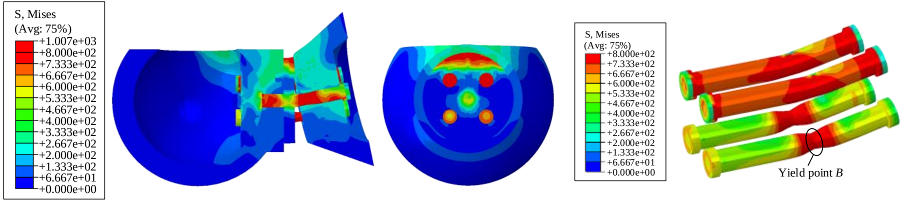

(b) BD8-8

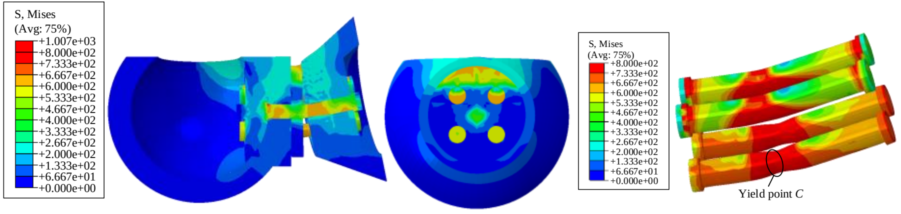

(c) BD8-9

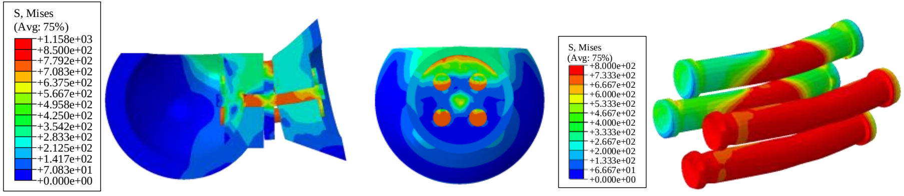

(d) BD8-10

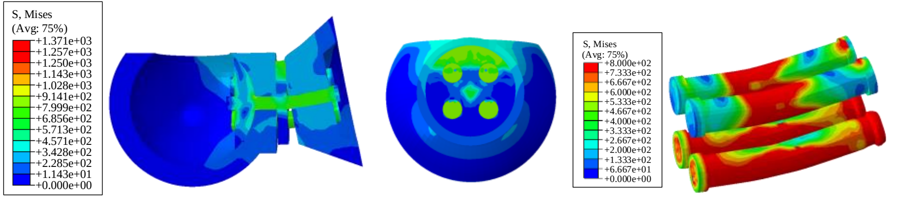

(e) BD8-11

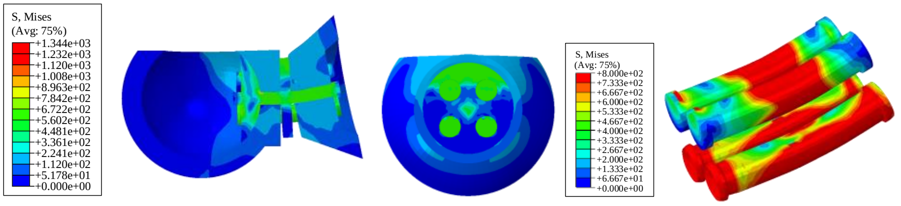

(f) BD8-12

Fig. 6 Mises stress contour diagrams of the sprayer joint with different diameters of the surrounding bolts

Table 3
Main characteristics of bending moment-rotation curves

Specimen ID	N_p (kN)	N_t (kN)	K_i (kN·m/rad)	M_u (kN·m)	θ_u (rad)	Specimen ID	N_p (kN)	N_t (kN)	K_i (kN·m/rad)	M_u (kN·m)	θ_u(rad)
Socket	0	0	227	4.22	0.158	——	——	——	——	——	——
BD8-7	0	0	4921	22.89	0.043	BD8-10	0	0	5037	35.99	0.158
BD8-7AP	100	0	5215	25.46	0.043	BD8-10AP	100	0	5283	37.22	0.148
BD8-7BP	200	0	5470	27.76	0.046	BD8-10BP	200	0	5503	38.38	0.121
BD8-7CP	300	0	5687	29.82	0.047	BD8-10CP	300	0	5693	39.53	0.101
BD8-7DP	400	0	5868	31.66	0.042	BD8-10DP	400	0	5856	40.42	0.089
BD8-7EP	500	0	6017	33.22	0.045	BD8-10EP	500	0	5990	40.99	0.078

BD8-7AT	0	100	4579	20.09	0.047	BD8-10AT	0	100	4761	34.74	0.170
BD8-7BT	0	200	4198	16.98	0.045	BD8-10BT	0	200	4453	33.47	0.176
BD8-7CT	0	300	3777	13.58	0.039	BD8-10CT	0	300	4114	32.07	0.180
BD8-7DT	0	400	3307	9.87	0.042	BD8-10DT	0	400	3747	30.64	0.187
BD8-7ET	0	500	2782	7.22	0.013	BD8-10ET	0	500	3352	29.24	0.202
BD8-8	0	0	4928	26.98	0.056	BD8-11	0	0	5041	40.02	0.235
BD8-8AP	100	0	5200	29.19	0.057	BD8-11AP	100	0	5262	40.92	0.176
BD8-8BP	200	0	5436	31.18	0.059	BD8-11BP	200	0	5467	41.83	0.145
BD8-8CP	300	0	5637	32.95	0.060	BD8-11CP	300	0	5649	42.47	0.119
BD8-8DP	400	0	5804	34.45	0.061	BD8-11DP	400	0	5803	42.79	0.092
BD8-8EP	500	0	6275	35.70	0.061	BD8-11EP	500	0	5929	42.78	0.081
BD8-8AT	0	100	4615	24.59	0.057	BD8-11AT	0	100	4774	39.04	0.203
BD8-8BT	0	200	4262	21.99	0.058	BD8-11BT	0	200	4489	37.93	0.211
BD8-8CT	0	300	3872	19.41	0.072	BD8-11CT	0	300	4174	36.77	0.216
BD8-8DT	0	400	3447	16.23	0.075	BD8-11DT	0	400	3836	35.29	0.223
BD8-8ET	0	500	3026	12.79	0.087	BD8-11ET	0	500	3472	33.95	0.227
BD8-9	0	0	4997	31.60	0.097	BD8-12	0	0	5100	44.27	0.244
BD8-9AP	100	0	5249	33.35	0.097	BD8-12AP	100	0	5329	45.09	0.201
BD8-9BP	200	0	5468	34.96	0.089	BD8-12BP	200	0	5534	45.40	0.181
8-9CP	300	0	5659	36.43	0.080	BD8-12CP	300	0	5716	45.34	0.132
BD8-9DP	400	0	5822	37.65	0.067	BD8-12DP	400	0	5873	45.21	0.099
BD8-9EP	500	0	5956	38.56	0.067	BD8-12EP	500	0	6002	44.71	0.084
BD8-9AT	0	100	4709	29.69	0.097	BD8-12AT	0	100	5919	43.35	0.231
BD8-9BT	0	200	4387	27.62	0.097	BD8-12BT	0	200	4578	42.38	0.237
BD8-9CT	0	300	4026	25.35	0.097	BD8-12CT	0	300	4055	41.27	0.239
BD8-9DT	0	400	3396	22.86	0.098	BD8-12DT	0	400	3954	40.05	0.243
BD8-9ET	0	500	3268	20.15	0.105	BD8-12ET	0	500	3606	38.68	0.250

Notes: N_p denotes the axial pressure, N_t denotes the axial tension, K_i denotes the initial stiffness, M_u denotes the ultimate bending moment, θ_u denotes the ultimate rotation angle, where the bolt radius of the socket joint is 12mm.

Table 3 provides the initial stiffness, stiffness during bolt yield, bending moment during bolt yield, ultimate rotation angle, and ultimate bending moment of the sprayer joint under different load scenarios. It demonstrates that compared to the 100kN axial compression, the yield stiffness of the 500kN axial compression at the surrounding bolt radii of 7mm, 8mm, 9mm, 10mm, 11mm, and 12mm increased by 31.49%, 27.14%, 23.62%, 21.32%, 18.51%, and 16.72%, respectively, and the bending moment of the bolt yield increased by 31.45%, 27.28%, 23.62%, 21.32%, 18.51%, and 16.69%, respectively. On the other hand, compared to the 100kN axial tension, the yield stiffness of the 500kN axial tension at the surrounding bolt radii of 7mm, 8mm, 9mm, 10mm, 11mm, and 12mm decreased by 95.05%, 81.38%, 70.23%, 62.23%, 55.14%, and 51.59%, respectively, and the bending moment of the bolt decreased by 95.04%, 81.41%, 70.22%, 62.21%, 55.11%, and 51.63%, respectively.

The axial compression and axial tension exert a significant influence on the ultimate bending moment and rotation angle of the sprayer joint. Table 3 demonstrates that, compared to the 100kN axial compression, the ultimate bending moment of the sprayer joints with surrounding bolt radii of 7mm, 8mm, 9mm, 10mm, and 11mm increased by 30.48%, 22.31%, 15.62%, 10.13%, and 4.54%, respectively, under the 500kN axial compression. Additionally, the ultimate rotation angle of the joints with a bolt radius of 12mm approximately increased by 0.84%. Moreover, the ultimate rotation angle of the joints with bolt radii 7mm and 8mm increased by 4.05% and 7.07%, respectively, while the ultimate bending moment of the joints with bolt radii around 9mm, 10mm, 11mm, and 12mm decreased by 30.93%, 47.29%, 53.97%, and 58.21%, respectively. Furthermore, when compared to the 100kN axial tension, the yield stiffness of the 500kN axial tension decreased by 64.06%, 47.98%, 32.13%, 15.83%, 13.04%, and 10.77% for surrounding bolt radii of 7mm, 8mm, 9mm, 10mm, 11mm, and 12mm. The ultimate rotation angle of the bolt radius 7mm decreased by 72.34%, while the ultimate bending moment of the bolt radius joints around 8mm, 9mm, 10mm, 11mm, and 12mm increased by 52.63%, 8.25%, 18.82%, 11.82%, and 8.23%, respectively. The above phenomena demonstrate that the sprayer joint exhibits satisfactory ductility. Enhancing the radius of the surrounding bolt and increasing the axial pressure will augment the ductility of the specimen. However, applying axial tension will diminish the ductility of the specimen. This is attributed to the alteration in the initial stress state of the specimen caused by the initial external load.

3.2. Failure mode

From the analysis in the previous section, it is evident that there is a significant necking phenomenon in the lower part of the surrounding bolt when the radius of the new sprayer joint is less than 10mm. Fig. 7 illustrates Mises stress contour of different groups of sprayer joints under various load schemas. As the bolt radius decreases, the yield point of the surrounding bolt shifts from points *C* to *B*, and eventually to point *A* when the radius is 7mm. The influence of load schemas on the bending stiffness and bearing capacity of the sprayer joints has been previously illustrated. It is worthy to note that load conditions not only affect bending properties previous mentioned but also have a substantial impact on the failure mode of the joints. Fig. 7(b) reveals that when the axial tension exceeds 300kN, the surrounding bolts yield prematurely, and the yield point occurs at *A*. For other loading conditions, the failure mode remains the yield of the surrounding bolts at point *B*. This suggests that the axial tension weakens the bearing capacity of the joint, thereby influencing its failure mode. Furthermore, in the limit state, the stress value at the failure point gradually increases as the axial force increases.

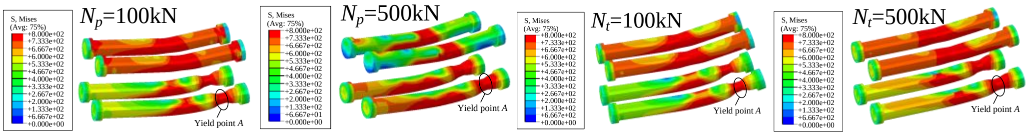

(a) BD8-7

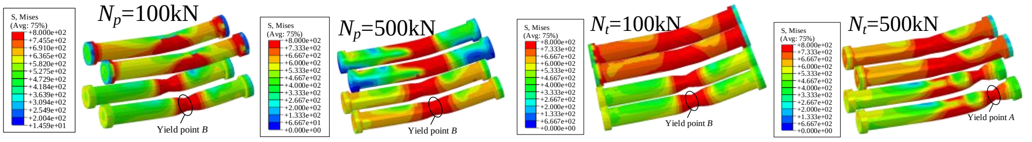

(b) BD8-8

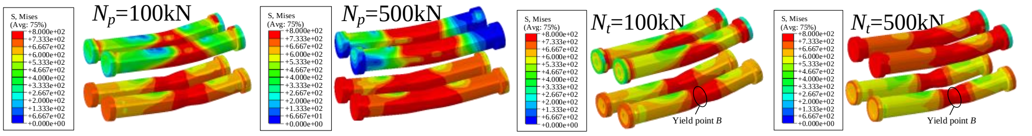

(c) BD8-9

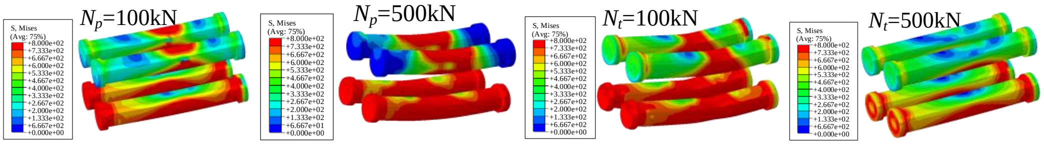

(d) BD8-10

Fig. 7 Mises stress contour of the sprayer joint under different load schemas

4. The establishment of the improved bending moment-rotation bilinear model of the joint and the derivation of the equation

4.1. Initial stiffness of the joint

The sixth-order polynomial fitting method is utilized to determine the initial stiffness of the joint by calculating the first-order derivative of the bending moment-rotation curve at the origin. The fitting result can be observed in Fig. 8 and satisfactory results are obtained.

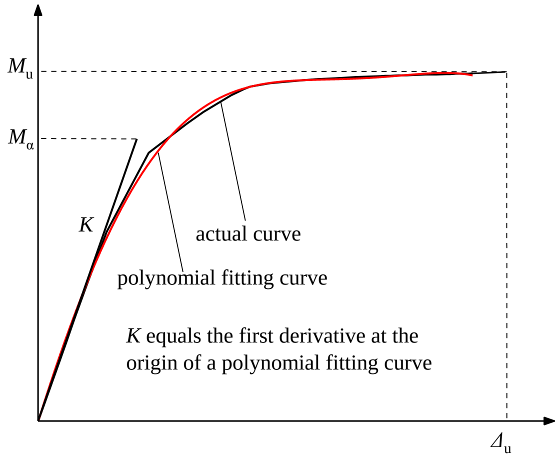

Fig. 8 Determination of initial stiffness

4.2. Modified yield coefficient

In the traditional model, parameters yield coefficient *a* and stiffness coefficient *b* are determined using the energy equivalent method where the area enclosed by the actual bending moment-rotation curve is made equal to the area enclosed by the simplified bilinear model. This method ensures energy conservation in seismic analysis by maintaining the same area through the geometric energy method. However, in static analysis, the bearing capacity of the reticulated shell is influenced by the initial stiffness and yield bending moment of the joints. The simplified bilinear model in the traditional method may encounter inaccuracy in basic static parameters such as initial stiffness and yield bending moment. Therefore, this paper proposes an improvement to the traditional method by obtaining the second derivative using the function relation of the bending moment-rotation angle curve. The yield point, which represents the minimum value of the second derivative, provides the real value of the yield bending moment M_α. The bilinear model is then modified by directly replacing the yield moment M_S obtained by the energy method with M_α.

The Fig. 9 depicts the modified bilinear model. In this model, the initial stiffness is denoted as *K* and the yield coefficient is represented as *A* (where the true value of the yield bending moment corresponds to the ultimate bearing capacity under bending moment). Additionally, the second stage in bilinear model is characterized by the stiffness coefficient *B*, then

$$A = M_\alpha / M_u \tag{1}$$

$$B = \left(M_u - M_\alpha\right) / \left(\Delta_u - M_\alpha / K\right) / K \tag{2}$$

where, *A* is the corrected yield coefficient, *B* is the corrected stiffness coefficient, M_u is the ultimate bending moment, M_α is the corrected yield bending moment, Δ_u is the rotation angle corresponding to the ultimate bending moment, and *K* is the initial stiffness.

The method described above is utilized to obtain the actual values of the yield bending moment M_α for the joints under varying surrounding bolt radii and loading schemas, as presented in Table 4. Subsequently, an improved bilinear model is developed for the sprayer joints with different surrounding bolt radii and loading schemas.

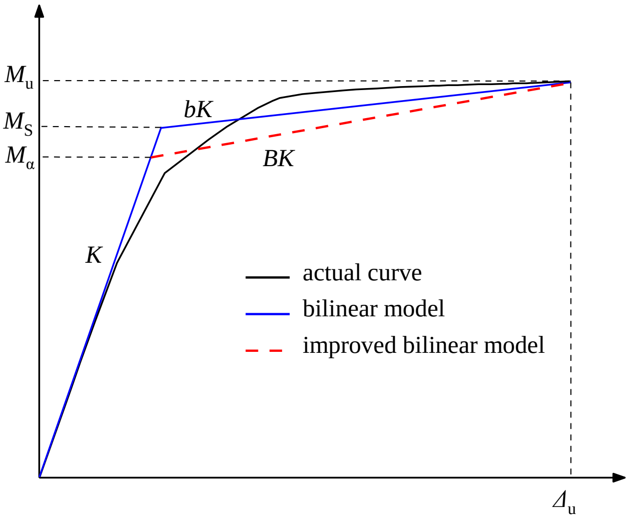

Fig. 9 Comparison between the improved bilinear model and the traditional one

4.3. Establishment of bilinear model

This section focuses on establishing a bilinear model using the radius of the surrounding bolt and the load conditions as parameter variables. The radius of the surrounding bolt is normalized by the maximal bolt radius, denoted as the dimensionless index m. Similarly, the load condition (measured in kN) is normalized by 500kN and recorded as the dimensionless index n. It is important that a positive value of n indicates the joint under compression, while a negative value indicates tension. The bilinear model is constructed following the method described in the previous section. The yield bending moment, the yield coefficient A and the stiffness coefficient B of the bilinear model is listed in Table 4.

Table 4
The value of yield bending moment, the yield coefficient A and the stiffness coefficient B of the bilinear model

SI	m	n	M_α	A	B	SN	m	M_α	A	B	SI	m	M_α	A	B
BD8-7	0.58	0	20.28	0.886	0.014	BD8-8	0.67	22.08	0.818	0.019	BD8-9	0.75	27.53	0.871	0.009
BD8-7	0.58	0.2	21.29	0.836	0.021	BD8-8	0.67	25.19	0.863	0.015	BD8-9	0.75	29.44	0.883	0.008
BD8-7	0.58	0.4	24.18	0.871	0.016	BD8-8	0.67	27.20	0.872	0.014	BD8-9	0.75	31.53	0.902	0.008
BD8-7	0.58	0.6	27.26	0.914	0.011	BD8-8	0.67	29.21	0.886	0.012	BD8-9	0.75	32.89	0.903	0.008
BD8-7	0.58	0.8	30.05	0.949	0.007	BD8-8	0.67	32.72	0.950	0.005	BD8-9	0.75	34.37	0.913	0.009
BD8-7	0.58	1	30.78	0.927	0.010	BD8-8	0.67	33.00	0.924	0.008	BD8-9	0.75	34.10	0.884	0.012
BD8-7	0.58	-1	16.91	0.842	0.016	BD8-8	0.67	20.41	0.830	0.017	BD8-9	0.75	25.07	0.844	0.011
BD8-7	0.58	-2	14.49	0.853	0.014	BD8-8	0.67	17.51	0.796	0.020	BD8-9	0.75	22.56	0.817	0.013
BD8-7	0.58	-3	11.15	0.821	0.018	BD8-8	0.67	15.16	0.781	0.016	BD8-9	0.75	19.95	0.787	0.015
BD8-7	0.58	-4	7.58	0.768	0.017	BD8-8	0.67	13.05	0.804	0.013	BD8-9	0.75	16.37	0.716	0.021
BD8-7	0.58	-5	4.09	0.566	0.098	BD8-8	0.67	9.28	0.726	0.014	BD8-9	0.75	13.45	0.667	0.020
BD8-10	0.83	0	31.76	0.882	0.006	BD8-11	0.92	34.94	0.873	0.004	BD8-12	1	37.88	0.856	0.005
BD8-10	0.83	0.2	33.63	0.904	0.005	BD8-11	0.92	37.02	0.905	0.004	BD8-12	1	39.47	0.875	0.005
BD8-10	0.83	0.4	34.96	0.911	0.005	BD8-11	0.92	38.00	0.908	0.005	BD8-12	1	41.12	0.906	0.004
BD8-10	0.83	0.6	36.16	0.915	0.006	BD8-11	0.92	37.96	0.894	0.007	BD8-12	1	40.88	0.902	0.006
BD8-10	0.83	0.8	36.60	0.905	0.008	BD8-11	0.92	37.79	0.883	0.010	BD8-12	1	40.30	0.891	0.009
BD8-10	0.83	1	36.11	0.881	0.011	BD8-11	0.92	37.11	0.867	0.013	BD8-12	1	39.06	0.874	0.012
BD8-10	0.83	-1	29.53	0.850	0.007	BD8-11	0.92	32.99	0.845	0.006	BD8-12	1	35.99	0.830	0.006
BD8-10	0.83	-2	27.05	0.808	0.008	BD8-11	0.92	30.54	0.805	0.008	BD8-12	1	33.62	0.793	0.008
BD8-10	0.83	-3	24.36	0.760	0.011	BD8-11	0.92	28.08	0.764	0.010	BD8-12	1	31.13	0.754	0.011
BD8-10	0.83	-4	22.29	0.727	0.012	BD8-11	0.92	25.22	0.715	0.012	BD8-12	1	28.50	0.712	0.012
BD8-10	0.83	-5	19.00	0.650	0.016	BD8-11	0.92	22.46	0.662	0.015	BD8-12	1	25.51	0.660	0.015

Notes: SI and M_α stands for Specimen ID and yielding bending moment (kN·m), respectively.

Yield coefficient A, stiffness coefficient B, initial bending stiffness K_i and yield bending moment M_α are nonlinearly fitted respectively using Eq. (3). The independent variables are surrounding bolt radius index m and load condition index n. The specific values of fitting coefficients are shown in Table 5.

$$T = a_{20}m^2 + a_{02}n^2 + a_{11}mn + a_{10}m + a_{01}n + a_{00} \qquad (3)$$

where T represents the fitting functions, and a_{20}, a_{02}, a_{11}, a_{10}, a_{01}, a_{00} represent the corresponding fitting coefficients. Table 5 shows the relevant parameters of nonlinear fitting of bilinear model, and Fig. 10 shows the corresponding fitting surface.

Table 5
Corresponding fitting coefficients of bilinear model

T	a_{20}	a_{02}	a_{11}	a_{10}	a_{01}	a_{00}
A	-0.047	-0.004	0.003	0.034	0.021	0.880
B	0.101	3.9E-4	0.008	-0.186	-0.008	0.090
K_i	1980.6	-17.55	-531.7	-3486.3	742.2	6680.8
M_α	-5.552	-0.174	-4.979	41.98	6.239	0.961

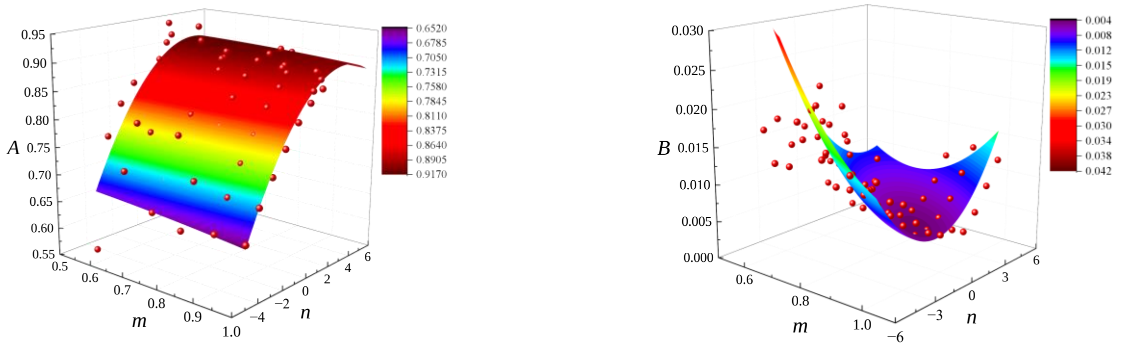

(a) A (b) B

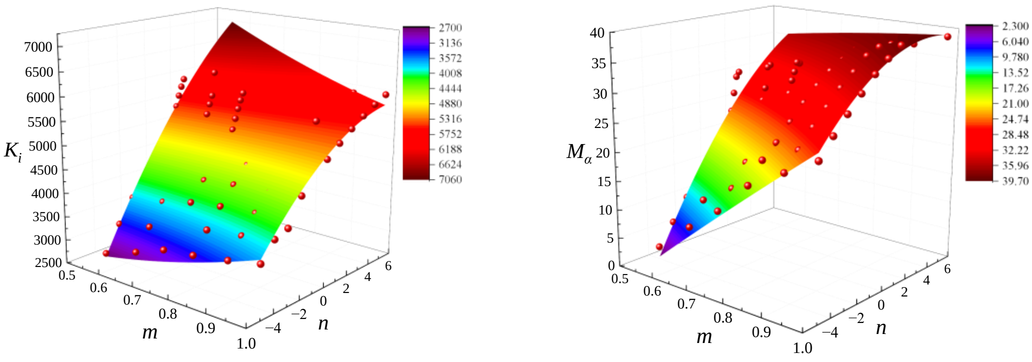

(c) K_i (d) M_α

Fig. 10 Bilinear model fitting surface diagram

4.4. Evaluation of Bilinear Models

In summary, the bending moment-rotation curve of the sprayer joint can be determined using Eq. (3) and Table 4 when the surrounding bolt diameter radius and loading schemas of the joint are known. This section evaluates the bilinear model. First, consistency between the original bending moment-rotation curve and the bilinear model is compared shown in Fig. 11, and it is evident that the A, B, bending stiffness, and yield moment provided by the bilinear model align well with the numerical results. Hence, it can be concluded that the estimation of the bilinear model can serve as a reference for a preliminary prediction of the bending moment-rotation curve of the sprayer joint.

Then, the prediction model is tested. The predicted values are obtained using the fitted formula and then plotted on a scatter diagram (shown in Fig. 12) with the true value as the T-axis and the predicted value as the T_{fit}-axis, which is normalized. The R-square values for A, B, bending stiffness, and yield bending moment are 0.884, 0.824, 0.935, and 0.958, respectively. The points on the scatter diagram predominantly fall along the ideal fitting line, indicating that the fitted formula can accurately calculate the main parameters of the bilinear model.

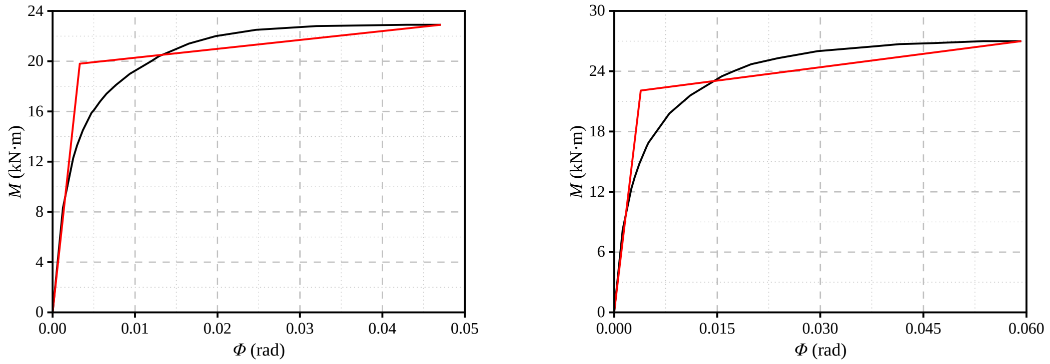

(a) BD-8-7 (b) BD-8-8

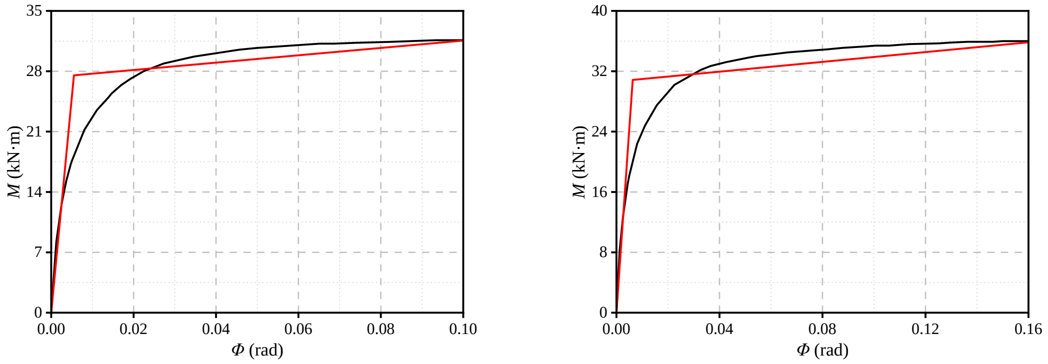

(c) BD-8-9 (d) BD-8-10

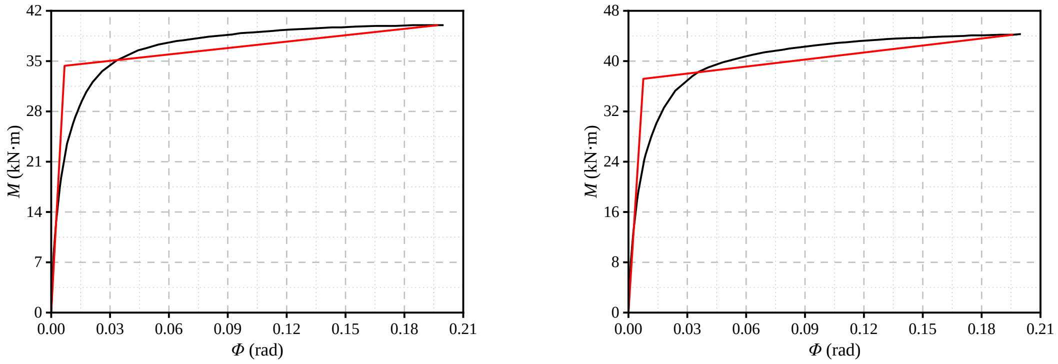

(e) BD-8-11 (f) BD-8-12

Fig. 11 Comparison of the bending moment-rotation curves between improved bilinear model and actual curve.

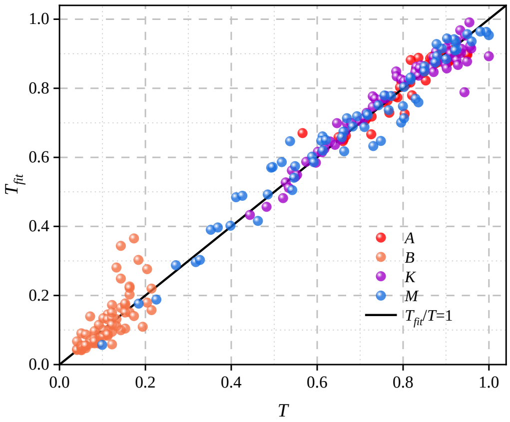

Fig. 12 Scatter diagram between actual values and predicted values

5. Semi-rigid reticulated shell with new sprayer joint

5.1. Modeling of semi-rigidly reticulated shell

The single-layer cylindrical reticulated shell, shown in Fig. 13, is selected to further investigate the bending performance of the new sprayer joint under a vertically uniform load. The joints located along the longitudinal side at the bottom of the reticulated shell are subjected to three-way constraints (i.e. hinged), while the joints at both ends experience vertical constraints. The shell members are made of circular tubes, denoted as C-100×5 (with a diameter of 100 mm and a thickness of 5 mm). The material is Q235 steel, and an isotropic, strain-hardening von Mises elastic-plastic model is used, while the elastic modulus is 2.1×10^{11} Pa, Poisson's ratio is 0.3, and the density is 7850 kg/m³. In this FE model, both geometric and material nonlinearities are considered, with the ultimate load of the reticulated shell determined using the arc-length method [39].

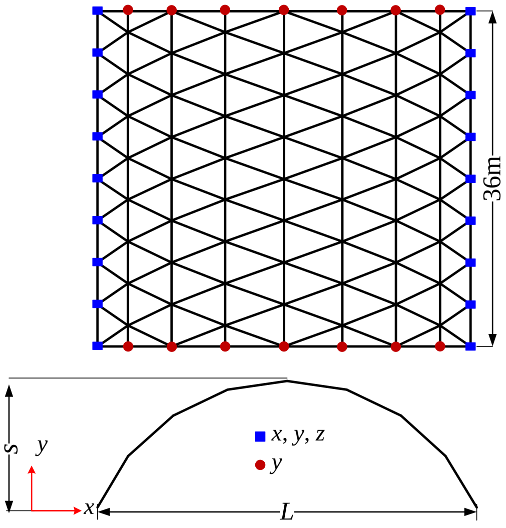

Fig. 13 Single-layer cylindrical reticulated shell model

To investigate the effect of joint stiffness on the load-carrying capacity of single-layer reticulated shells, this study employs a semi-rigid joint model, as shown in Fig. 14 [40]. Each member of the reticulated shell is modeled using 10 beam elements, as illustrated in Fig. 14(a). The distance between the centers of two joints *i*' and *j*', denoted as *l*, is considered. To account for joint size, two rigid beams are attached at both ends of each member, with a length equal to the diameter of the joint, denoted as $2\lambda l$. The actual length of the member is $(1\text{-}2\lambda)l$, where λ represents the joint size and is much smaller than 0.5. In this study, 2λ is set to 0.06. To simulate the semi-rigidity of the joint, two types of spring elements (the linear Combin14 and nonlinear Combin39 elements in the ANSYS package) are used to connect the ordinary and rigid beams, as shown in Fig. 14(a). In the ANSYS package, both the ordinary and rigid beams are modeled using the Beam188 element, which is suitable for analyzing slender to moderately stubby/thick beam structures and accounts for shear deformation effects, based on Timoshenko beam theory. The elastic modulus of the ordinary beam is assigned the actual value corresponding to the steel material used, while the elastic modulus of the rigid beam is increased by a factor of 1000 to represent infinite joint stiffness.

Fig. 14(b) illustrates a joint connecting six members, while the semi-rigid joint is simulated using both the linear spring element Combin14 and the nonlinear Combin39. At the junction of the ordinary and rigid beams, there are two coincident nodes. One node belongs to the ordinary beam, while the other one belongs to the rigid beam. These two nodes have the same coordinates, indicating that they coincide and the length of the spring element is zero. For each junction between the ordinary and rigid beams, a total of six springs are used. Three of springs are used to simulate translational stiffness (specifically, one axial stiffness K_{ax} and two shear stiffness K_{sy} and K_{sz}, as shown in Fig.14(b)), while the remaining three springs are used to simulate rotational stiffness (namely, two bending stiffness K_{by} and K_{bz}, and one torsional stiffness K_{tx}). In the typical joint area shown in Fig. 14(b), a total of 36 springs are present in the system, effectively simulating a semi-rigid joint. K_{bz} is simulated by nonlinear Combin39 element, while other stiffness are simulated by linear Combin14 element. According to the existing researches [40, 41], the bending stiffness K_{bz} of the strong axis of the joint has a significant effect on the bearing capacity of the reticulated shell, while other stiffness (axial, shear, torsion, weak axis bending stiffness) has slight effect. Therefore, the bending stiffness K_{bz} (Combin39) of the strong axis is taken from the bending moment-rotation angle curve obtained in Section 3 when carry out numerical calculation of the semi-rigid reticulated shell, while the stiffness of the other five types of stiffness (Combin14) is taken as a large value 10^{15} representing infinite stiffness.

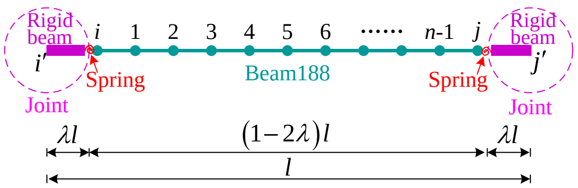

(a) semi-rigidly jointed model

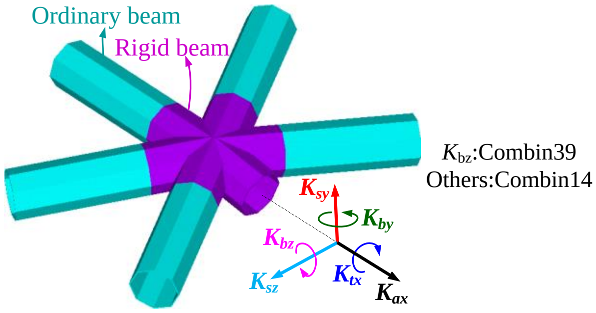

(b) illustrative diagram of different joint stiffness

Fig. 14 Mechanical model considering joint size and joint semi-rigid stiffness

5.2. Stability analysis of reticulated shell with new sprayer joint

To systematically investigate the comparative performance of the new sprayer joint (i.e. BD-8-8) and the traditional socket joint in single-layer cylindrical reticulated shells, this section presents a comprehensive parametric study considering 100 spans of the reticulated shell. Table 6 summarizes the geometric parameters of the reticulated shell considered in the present parametric study. The bending moment-rotation curves obtained in Section 3 are imported into the ANSYS package (i.e. the semi-rigidly modeled reticulated shell described in Section 5.1), where the comparative performance of the new sprayer joint and the traditional socket joint in single-layer cylindrical reticulated shells is analyzed in detail.

Table 6
Parametric study of cylindrical reticulated shell with new sprayer joint

Joint	Span *L*/m	Rise-to-span ratio s/*L*	No.
New sprayer joint	30–70	1/3	100
Socket joint	30–70	1/3	100
Summary			200

The ultimate load of reticulated shells with different spans was obtained using the arc-length method, considering both material and geometric nonlinearity. The ultimate load of reticulated shells with sprayer joints was normalized by the ultimate load of rigid reticulated shells and plotted against the parameter of the reticulated shells (i.e. span), as shown in Fig. 15. The results revealed that (i) the ultimate load of the new sprayer joint reticulated shell has significantly increased compared to the traditional socket joint, indicating an efficient and successful design approach for the new sprayer joint, and (ii) the bending stiffness of the new sprayer joint reticulated shell with a large span has a greater influence on the bearing capacity of the reticulated shell. The typical failure mode of the new sprayer joint reticulated shell is shown in Fig. 16. The single-layer cylindrical reticulated shell is observed to fail due to local joint failure combined with flexural buckling of the members, as depicted in Fig. 16.

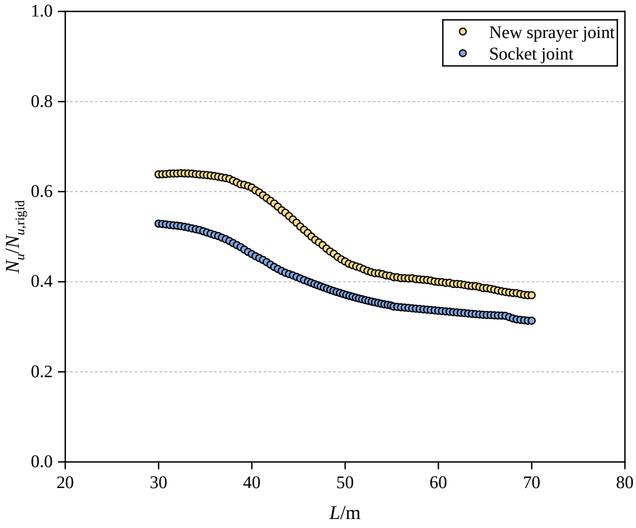

Fig. 15 Ultimate load of reticulated shells with sprayer joints and socket joint normalized by that of the rigid shell

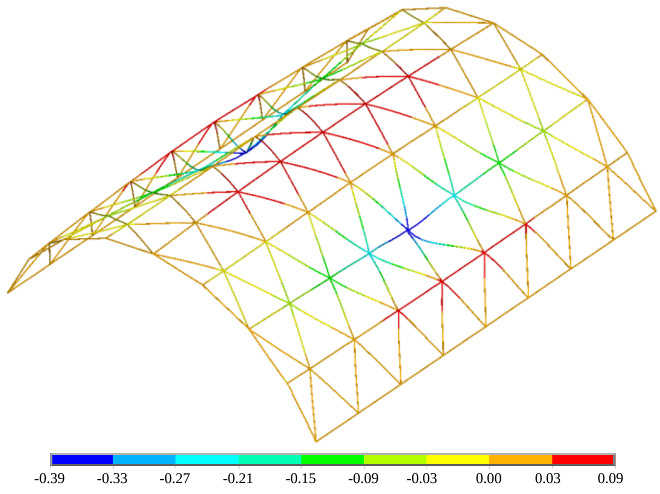

(a) L=30m, s/L=1/3

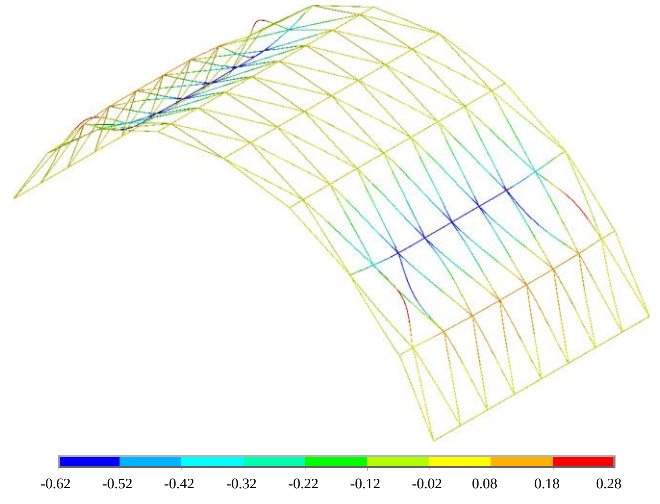

(b) L=70m, s/L=1/3

Fig. 16 Typical failure mode of reticulated shell with sprayer joint

6. Conclusion

This paper develops a novel sprayer joint that features a more rational force transmission mechanism. Initially, the joint is designed, followed by finite element simulation and mechanical analysis. Subsequently, the bending performance of the new sprayer joints under various surrounding bolt radii and load schemas is investigated. The improved bilinear model is established to depict the bending moment-rotation curve by parametric study. Finally, the comparative performance of the new sprayer joint and the traditional socket joint in single-layer cylindrical reticulated shells is studied in detail. The main research contents and conclusions of this study are summarized as follows:

(1) The new sprayer joint exhibits a considerable enhancement in bending stiffness and ultimate bending moment compared with the socket joint, with a slight increase in material cost.

(2) The surrounding bolt radius and load conditions have a substantial effect on the bending performance of the new sprayer joints. As the bolt radius increases, the initial stiffness remains relatively constant, while the ultimate bending moment significantly increases, resulting in a shift in failure mode. Moreover, axial compression boosts the initial stiffness and ultimate bearing capacity, postponing bolt necking, whereas axial tension diminishes these characteristics and triggers premature yielding of surrounding bolts under particular circumstances.

(3) The improved bilinear mode is proposed, and the bending moment-rotation curve of the sprayer joint can be determined by developed equation when the surrounding bolt diameter radius and loading schemas of the joint are known. Bending stiffness and yield moment provided by the bilinear model align well with the numerical results. The proposed bending moment-rotation curve effectively characterizes the bending performance of the joint, thereby offering valuable insights for joint design and application.

(4) The comparative performance of the new sprayer joint and the traditional socket joint in single-layer cylindrical reticulated shells is analyzed in detail. The results revealed that (i) the ultimate load of the new sprayer joint reticulated shell has significantly increased compared to the traditional socket joint, indicating an efficient and successful design approach for the new sprayer joint, and (ii) the bending stiffness of the new sprayer joint reticulated shell with a large span has a greater influence on the bearing capacity of the reticulated shell.

Acknowledgements

This work was supported by National Natural Science Foundation of China (No.51408490), Natural Science Basic Research Program of Shaanxi (2022JM-234), Training Programs of Innovation and Entrepreneurship for Undergraduates (202310712067, 202410712019), are gratefully appreciated.

Declarations

Conflict of interest: No potential conflict of interest was reported by the authors.

Reference

[1] Fan F., Ma H., Chen G. and Shen S., “Experimental study of semi-rigid joint systems subjected to bending with and without axial force”, Journal of Constructional Steel Research, 2012, 68(1), pp.126-137.

[2] Fan F., Ma H., Cao Z. and Shen S., “Direct estimation of critical load for single-layer reticulated domes with semi-rigid joints”, International Journal Space Structure, 2010, 25(1), pp.15-24.

[3] Zhang X., Li H., Yu X. and Han J., “Research on stiffness and bilinear model of hub-shape inlay joints”, Spatial Structures, 2022, 28(2), pp.56-62.

[4] Xiao Z., Li R., Li H., Bi S. and Li B., “Effect of joint stiffness on the load- carrying capacity of single-layer cylindrical reticulated shell with improved bolt-column (IBC) joint”, Thin-Walled Structures, 2024, 198, pp.111691.

[5] Elhout E., “Effect of beam-column connection types on the response modification factors of steel frames”, International Journal of Steel Structures, 2024, 24(1), pp.132-143.

[6] Fan J., Wu Z., Liu J., Wang, Y., Zheng, H. and Tee, K., “Damage and failure of semi-rigid steel joints during progressive collapse”, Structures, 2023, 58, pp.05632.

[7] Gou B., Wang X., Wu C. and Wang R., “Experimental investigation of aluminium alloy gusset joints' dynamic response to lateral impact loads: Evaluating the influence of gusset plate bending stiffness”, Structures, 2024, 62, pp.106288.

[8] Qi L., Yuan Z. and Xue J., “Experimental and numerical study on seismic performance of steel semi-rigid joints equipped with SMA bars and friction dampers”, Engineering Structures, 2024, 301, pp.117320.

[9] Xiao Z., Li R., Li H., Yan G., Fan R. and Jiang S., “Effect of joint behaviors on the load-carrying capacity of single-layer reticulated dome”, Structures, 2024, 68, pp.107124.

[10] Reinosa J., Loureiro A., Gutierrez R. and Lopez, M., “Artificial neural network prediction of the initial stiffness of semi-rigid beam-to-column connections”, Structures, 2023, 56, pp.104904.

[11] Tan Y., Zhang Y., Zhang Q. and Fan F., “Structural performance of a novel combined nested bolted joint for aluminum alloy mega-latticed structures”, Structures, 2023, 57, pp.105246.

[12] Wang X., Lu G., Liu Y., Chen Z., An Q. and Wang X., “Lateral stiffness of modular steel joint

with semi-rigid bolted intra-module connection", Journal of Building Engineering, 2024, 97, pp.110668.

[13] Wu Z., Lu X., Bao H., Li L. and Lu Z., "Experimental response of semi-rigid reinforced concrete beam-column joints with bolted angle dissipating connections", Journal of Building Engineering, 2024, 90, pp.109345.

[14] Yao H. Huang Y., Ma W., Liang L. and Zhao Y., "Dynamic analysis of a large deployable space truss structure considering semi-rigid joints", Aerospace, 2023, 10(9), pp.821.

[15] Xiao Z., Li R., Li H., Luo G. and Li B., "Research on bending performance and bilinear model of an improved bolt-column (BC) joint", Advanced Steel Construction, 2024, 20, pp.3-10.

[16] Dong S., Yu Y., Ge H. and Luo Y., "Nonlinear dynamic collapse analysis of space semi-rigid frames using finite particle method", Journal of Constructional Steel Research, 2024, 216, pp.108607.

[17] Jiao Z., Cui L., Liu H., Wei J., Xu D. and Bao Y., "Design and numerical analysis of new earthquake-resilient semi-rigid joints", Journal of Constructional Steel Research, 2024, 213, pp.108393.

[18] Lemes I., Silveira R., Teles L. Barros R. and Silva A., "Numerical formulation for advanced non-linear static analysis of semi-rigid planar steel frames", Journal of the Brazilian Society of Mechanical Sciences and Engineering, 2023, 45(7), pp.358.

[19] Liu D., Zheng Y., Wang Z., Pan J., Hu, S. and Yin T., "Boundary-oriented optimization of semi-rigid connections in steel frames using BNSGA", Journal of Constructional Steel Research, 2024, 214, pp.108471.

[20] Lu S., Wang M., Han X. and Yin T., "Seismic performance analysis of semi-rigid steel frame based on panel zone mechanical characteristics of the joint experiment study", Ksce Journal of Civil Engineering, 2024, 28(5), pp.60-79.

[21] Ma H., Zhao C., Jiang Y., Zhou J. and Wang Y., Rotational resistance test of a new aluminum alloy penetrating (AAP) joint system", Advanced Steel Construction, 2023, 19(2), pp.121-129.

[22] Li R., Su A., Wang Y. and Zhao O., "Geometric analysis and local buckling behavior of wire arc additively manufactured ER110S cruciform section stub columns", Engineering Structure, 2025, 322, pp.118819.

[23] Petrovic M., Pavicevic D., Ilic I., Terzovic J. and Sekularac N., "Elements of a timber lamella structure: analysis and systematization of joints", Buildings, 2023, 13(4), pp.885.

[24] Wang G., Zhuo X., Zhang S. and Wu J., "Study on the mechanical properties and design method of frame-unit bamboo culm members based on semi-rigid joints", Buildings, 2024, 14(4), pp.991.

[25] Xiao S., He Y., Golea T., Denoël V. and Demonceau J., "Simplified methods to predict the robustness of steel parking-structure joints", Journal of Constructional Steel Research, 2024, 213, pp.108355.

[26] Yu J., Zhao C., Zhong W., "Seismic behavior of partially encased composite columns-steel plate shear wall structure with different semi-rigid joints", Journal of Building Engineering, 2024, 82, pp.108177.

[27] Feng F., Ma H. and Shen S., "Numerical simulation and experimental study on mechanical characters of bolt-ball joint system", Engineering Mechanics, 2009, 26(12), pp.92-99.

[28] Zhang X., Li H., Chen X., Zhu Z. and Yu X., "Research on stiffness of hub-shape inlay joint and bearing capacity of single-layer spherical reticulated shell", Engineering Mechanics, 2022, 39(9), pp.179-190.

[29] Guo X., Zhu S., Xiong Z. and Luo Y., "Design method for buckling capacity of K6 single-layer reticulated shells with aluminum alloy gusset joints", Journal of Building Structures, 2017, 38(7), pp.16-24.

[30] Fan F., Ma H., Chen G. and Shen S., "Experimental study of semi-rigid joint systems subjected to bending with and without axial force", Journal of Constructional Steel Research, 2012, 68(1), pp.126-137.

[31] Ma H., Fan F., Chen G., Chao Z. and Shen S., "Numerical analyses of semi-rigid joints subjected to bending with and without axial force", Journal of Constructional Steel Research, 2013, 90, pp.13-28.

[32] Shi M., Xiang P. and Wu M., "Experimental investigation on bending and shear performance of two-way aluminum alloy gusset joints", Thin-Walled Structures, 2018, 122, pp.124-136.

[33] Wu F. and Chen W., "A design model for semi-rigid connections", Engineering Structures, 1990, 12(2), pp.88-97.

[34] Ma H., Ren S. and Fan F., "Parametric study and analytical characterization of the bolt-column (BC) joint for single-layer reticulated structures", Engineering Structures, 2016, 123, pp.108-123.

[35] Frye M. and Morris G., "Analysis of flexibly connected steel frames", Canadian Journal of Civil Engineering, 1975, 2(3), pp.280-291.

[36] Mohammad R., Hoshyar N. and John E., "Proposed mathematical model for semi-rigid joint behaviour (M-θ) in space structures", International Journal of Space Structures, 2014, 29(2), pp.71-80.

[37] Chen W. and Kishi N., "Semi-rigid steel beam-to-column connections: data base and modeling", Journal of Structural Engineering, 1989, 115(1), pp.105-119.

[38] Li R., Xiao Z., Li, H. and Li B., "Research on bending stiffness of the new sprayer joint", International Journal Steel Structure, 2024, 24, pp.256-263.

[39] Zhao C., Zhou Y., Wang G., Li H. and Wang Y. "Calculation method of the bearing capacity of a novel modular joint of an aluminium alloy lattice shell structure", Structures, 2021, 34, pp.3268-3282.

[40] Li H. and Taniguchi Y., "Effect of joint stiffness and size on stability of three-way single-layer cylindrical reticular shell", International Journal of Space Structures, 2020, 35(3), pp.90-107.

[41] Li H. and He S., "Stability of semi-rigid jointed space truss considering member instability", Spatial Structures, 2019, 25(04), pp.18-26.